Continuous subsurface velocity measurement with coda wave interferometry

Baoshan Wang,[1] Ping Zhu,[1] Yong Chen,[1] Fenglin Niu,[2] and Bin Wang[3,4]

[1] A 1-month field experiment was conducted near Kunming in Yunnan Province, China, to continuously monitor subsurface velocity variations along different baselines. The experiment site is located 10 km west to the seismically very active Xiaojiang fault zone. An electric hammer was used as a source to generate highly repeatable seismic waves, which were recorded by 5 short-period seismometers deployed at ~10 m to 1.2 km away from the source. Velocity variation was estimated by using coda wave interferometry technique. The technique measures changes in differential time between the coda and the first arrival, which is in principal insensitive to timing errors. We obtained a fractional velocity perturbation ($\delta v/v$) of 10^{-3} to 10^{-2} with a precision of 10^{-4}. The measured velocity variation is consistent among different components and stations and appears to well correlate with deep water level. The velocity variation is featured by a long-term linear trend and well-developed daily cycles. The latter is interpreted as the velocity response to the barometric pressure. A multivariate linear regression analysis of the data indicates that the velocity change exhibits a negative correlation with barometric pressure, with a stress sensitivity of 10^{-6}/Pa at the experimental site.

1. Introduction

[2] The time-varying stress state of fault systems at seismogenic depths is perhaps the single most important property controlling the sequencing and nucleation of seismic events. The measurement of stress, however, is notoriously difficult, particularly at seismogenic depths. Numerous laboratory studies over the last several decades have shown that the seismic velocity of crustal rocks clearly exhibit stress dependence with a stress sensitivity of 10^{-9} to 10^{-8} Pa^{-1} [e.g., *Birch*, 1960, 1961; *Simmons*, 1964]. Such dependence is attributed to the opening/closing of microcracks in response to changes in the stress normal to the crack surface [e.g., *Walsh*, 1965; *Nur*, 1971]. Thus stress changes can, in principle, be detected through measuring changes of seismic velocity. Indeed there have been many attempts to accomplish this goal [e.g., *De Fazio et al.*, 1973; *Reasenberg and Aki*, 1974; *Leary et al.*, 1979; *Yukutake et al.*, 1988; *Yamamura et al.*, 2003; *Silver et al.*, 2007]. The fractional change in seismic velocity with respect to stress change appeared to spread over a wider range, from 10^{-9} to 10^{-6} Pa^{-1}.

[3] The small change of seismic velocity is usually estimated through measuring the subtle changes in absolute travel time of the first arrival along a fixed source-receiver path. Precisions in travel time measurement is thus of key importance to the success of these field experiments. One potential error source is timing. Using the first arrival time to estimate velocity perturbation thus suffers from systematic timing errors in the digitizer's base clock and in triggering time. Temperature fluctuation is observed to have notable effects on the measured travel time of the first arrival [*Leary et al.*, 1979; *Silver et al.*, 2007].

[4] Coda waves in the later part of a seismogram are generally considered to be generated by multiple scattering/reflection in the crust [*Aki and Chouet*, 1975; *Wegler*, 2004]. Since the pioneering study of *Aki* [1969], decay of coda waves has been extensively analyzed to study the attenuation property of crustal rocks (see *Herraiz and Espinosa* [1987] and references therein). Meanwhile coda waves are also better tools to image subtle changes of crustal rocks as they sample the medium multiple times which effectively amplifies any small changes in the medium. More importantly the differential times between coda waves and the first arrival are essentially insensitive to timing errors discussed in the previous paragraph. Thus one can apply the interferometry technique to the coda waves in the consecutive recordings to detect subtle crustal changes. A generalized theory of coda wave interferometry was recently proposed by *Snieder et al.* [2002] and *Snieder* [2006] and its effectiveness has been well demonstrated in ultrasonic experiments [*Snieder et al.*, 2002; *Grêt et al.*, 2006b]. The technique has been widely applied to field experiments

---

[1]Institute of Geophysics, China Earthquake Administration, Beijing, China.
[2]Department of Earth Science, Rice University, Houston, Texas, USA.
[3]School of Earth and Space Sciences, University of Science and Technology of China, Hefei, China.
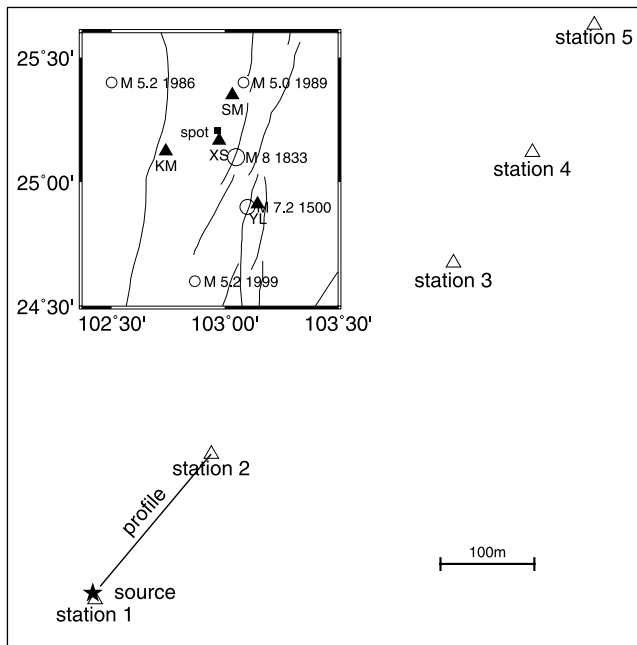[4]Earthquake Administration of Yunnan Province, Kunming, China.

Figure 1. Map of the experiment site. Locations of the source and stations are indicated by solid star and open triangles, respectively. The solid straight line shows the geophone survey profile. The profile starts with an offset of 15 m and extends to 250 m far away from the source, which coincides with the 2nd station. Inset shows the major earthquakes (open circles) occurred around the experiment site, as well as the geodetic stations (solid triangles) that measure ground water level (XS), gravity (KM), and barometric pressures (KM, SM). Temperature is recorded at stations SM and YL. The experiment site is indicated by a solid square.

involving both active and passive source data. For example, it has been used to monitor in situ velocity changes caused by artificially controlled stress in mining environments [*Grêt et al.*, 2006a], as well as to detect velocity changes along fault zones [*Poupinet et al.*, 1984] and volcanic areas [*Ratdomopurbo and Poupinet*, 1995; *Matsumoto et al.*, 2001; *Wegler et al.*, 2006]. It has also been successfully used to image changes in the scattering field associate with aseismic events [*Niu et al.*, 2003] and to monitor magma propagation in an active volcano setting [*Grêt et al.*, 2005]. In this study, we applied the coda wave interferometry technique to monitor in-situ seismic velocity variations caused by natural loadings (e.g., solid earth tide and barometric pressure).

[5] Ground water levels in the deep wells were observed to respond to stress changes caused by solid earth tide, barometric pressure [e.g., *Spane*, 2002] and large earthquakes [e.g., *Montgomery and Manga*, 2003]. *Silver et al.* [2007] suggested that the water levels affect pore pressure of subsurface rocks and further affect the seismic velocity. *Sens-Schönfelder and Wegler* [2006] found that fluctuation in ground water level caused by precipitation appears to be able to qualitatively explain the seasonal variation of the subsurface velocity field. In this study, a field experiment was conducted close to a deep well with continuous ground

water level record, which allows us to calibrate the velocity more precisely than most of the previous studies.

2. Field Experiment

[6] The field experiment was conducted near Kunming in the southeast China, during the period from 22:30 pm of 7 April (local time) to 23:30 pm of 8 May 2006. We selected the site for several considerations. The experiment site is located at a peak of anticline about 10 km west to the Xiaojiang fault (Figure 1), an active fault zone with high seismicity. More than six earthquakes with magnitude >5 occurred within the fault zone from 1 January 2005 to 25 August 2006. There are plentiful outcrops of highly fissured Devonian lime stones [*Song et al.*, 1998] in the experimental site, and the overburden unconsolidated sediments there is no thicker than 2 m. The site possesses various geodetic records so that we can obtain observations of tidal and barometric strains as well as tectonically related strains. A 2000-m deep water well can be found about 1.2 km south from the experiment site (solid triangle labeled with XS in Figure 1). There are temperature recording in YL station, precipitation and barometric pressure recordings in SM station, and temperature, barometric pressure and gravity data in KM station. All stations are located within 30 km from the experiment site. Barometric pressure, temperature and gravity measurements are sampled continuously every one hour, and the water level is recorded once every one minute.

[7] We used the ESS200 electronic hammer (manufactured by GISCO) as the seismic source to generate highly repeatable shots. When detonated, the hammer hits on a square iron plate with a dimension of 30 cm × 30 cm × 2 cm that was fixed on the ground surface. To minimize the noises caused by seasonal wind during the day time, our regular experiment was conducted in the night time from 7 April 2006 to 5 May 2006. The source was detonated 6 times a day at 00:30, 01:30, 06:30, 07:30, 22:30 and 23:30, respectively. During the last two days of the experiment (between 10:30 am of 5 May to 01:30 am of 7 May) we repeated experiment once per hour, hereafter referred as a densely sampled experiment. For each recording, a total of 30 and 10 shots, respectively, were fired within 12 minutes for the regular and densely sampled experiments. Their records were linearly stacked to enhance the signal-to-noise ratio (SNR).

[8] Two types of recorders were deployed: a surveying line (thick line in Figure 1) consisting of 48 geophones with offset ranging from 15 m to 250 m at 5 m spacing; and 5 three-component short-period seismometers (open triangles in Figure 1) in the distance range of ∼10 m−1.2 km from the source. The geophones have a dominant frequency of around 60 Hz and have a relatively flat response in the frequency range of 10 Hz to 200 Hz. The "StrataVisor NZ" manufactured by Geometrics was used as the acquisition system for the geophone line. The geophones and seismometers were deployed on the sediments and the outcrops of bedrock, respectively. For each recording, individual traces of the 30 or 10 shots were aligned with the triggering time and linearly stacked in the acquisition system. The data were collected at a sampling rate of 32,000 samples per second with a record length of 0.512 second. The digitizer is
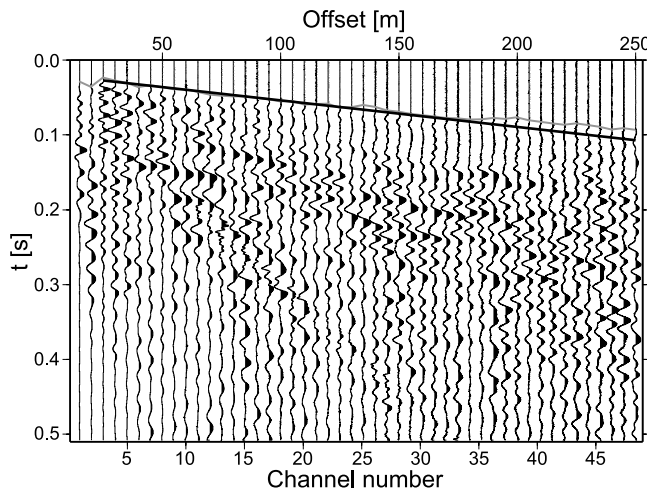
Figure 2. Stacked seismic profile recorded by geophones at 01:30 am of 13 April 2006. The gray line indicates the manually picked first arrivals, and the black line is the best linear fitting of the data from a model with a P wave velocity of 2.8 km/s.

continually sampling the data, and receives a trigger that will generally be between two digitized samples. The time series is interpolated and re-sampled so that the time series begins at the time of the trigger with an accuracy of 1/32 of the sample interval (Geometrics Engineering, personal communication, 2006). The seismometers have a natural frequency of 1 Hz with a flat frequency response up to 40 Hz. Response at frequencies higher than 60 Hz was not calibrated. The seismograms were continuously digitalized by a 24-bit digitizer and recorded with a sampling rate of 500 samples per second and the acquisition system is timed by a GPS clock.

[9] A total of 218 recordings was obtained throughout the experiment period from 7 April to 8 May 2006. During the 1-month period there was a 3-day period of continuous rainfall in the experiment site and surrounding regions. A typical seismic profile recorded from the surveying line is shown in Figure 2. The survey line here is designed to constrain the basic information, such as the P-wave velocity, of the experiment site rather than to obtain detailed geological structure. A complicated first arrival time curve is obtained from the profile. For example the first arrivals recorded at channels 1 and 2 come later than that of channel 3. No clear reflectors can be identified from the profile. The complexity of the seismic profile may indicate that the crust beneath the experiment site is fairly heterogeneous. Through linearly fitting of the travel time of the first arrivals in the distance range of 25–125 m, we obtained an average P wave velocity of ~2.8 km/s (thick line in Figure 2).

3. Measuring Velocity Variation Using Coda Wave Interferometry

3.1. Coda Wave Recording

[10] As indicated in Figure 2, the upper crust in the experiment site appears to be remarkably heterogeneous. The recorded large amplitude coda waves resulting from multiple scattering [Aki and Chouet, 1975] are ideal for coda wave interferometry. As the record length of the geophones (0.512 second) is too short to document the entire coda wavefield, we thus only used the seismograms recorded by the five short-period seismometers in this study. Figure 3 shows the stacked waveforms recorded at two closest stations to the source (stations 1 and 2 in Figure 1). The amplitude spectra of stacked waveform are also shown in Figures 3e and 3j for stations 1 and 2, respectively. The spectra of station 1 show a prominent peak at ~77 Hz on all of the three components and a second peak at ~70 Hz on the E-W and N-S components (Figure 3e). At station 2, all of the three components show a peak at ~72 Hz, while the U-D and E-W components have another peak at ~82 Hz. These harmonic signals appeared to be the dominant components of the observed coda waves. Narrow-band coda waves were also found by Grêt et al. [2006a] in their active source experiment.

[11] As both of the narrow peaks fall in the uncalibrated frequency range of the short-period sensors, one might ask whether they are true signals or instrument related parasitic auto oscillations. To verify the high-frequency response of the short-period sensors, we compared their spectra with those of the geophone records (Figure 4). The spectra were calculated using exactly the same time window, the first 0.512 second of the records of the two stations and two geophone channels. In general the spectra computed from the two types of sensors agree very well with each other. The two adjacent sensors, channel 48 and station 2 (Figure 1), essentially have the same spectrum. The high-frequency peak between 70 and 80 Hz is shown in all of the four spectra. We thus believe that they are true signals and any subtle changes in their arrival times reflect temporal variations in the scattering field.

[12] To enhance the SNR of the coda waves, bandpass filters of 73–78 Hz and 69–75 Hz were used to filter the seismograms of stations 1 and 2, respectively. An example of the filtered three-component waveforms is shown in Figures 3b–3d and 3g–3i for stations 1 and 2, respectively. The envelope of the filtered coda waves decays exponentially with time after 0.1 second and 0.3 second for stations 1 and 2, respectively, indicating that the observed coda waves are indeed resulting from multiple scattering [e.g., Aki and Chouet, 1975]. The calculated SNR of the unfiltered waveforms recorded at station1 (Figure 3a) is >5 from a time window even 3 seconds after the first arrival (insets in Figure 3a). We found that in general SNRs of the coda waves are >50 for station 1 and >5 for station 2, respectively. The amplitude of coda waves, however, decays rapidly with source-receiver distance. We found that the coda waves recorded by the three farthest stations are not strong enough for interferometry analysis. Thus we will focus on the stations 1 and 2 hereafter. On the basis of the SNR, we applied the coda wave interferometry technique to the entire 3-second records of station 1 and only the first 1.5 seconds for station 2.

3.2. Estimation of Velocity Variation With Coda Wave Interferometry

[13] We first aligned the bandpass filtered seismograms at each station recorded from different shots to the first arrival. A comparison of the seismograms from two different shots is shown in Figure 3 (solid line for the 22:30 of 7 April shot
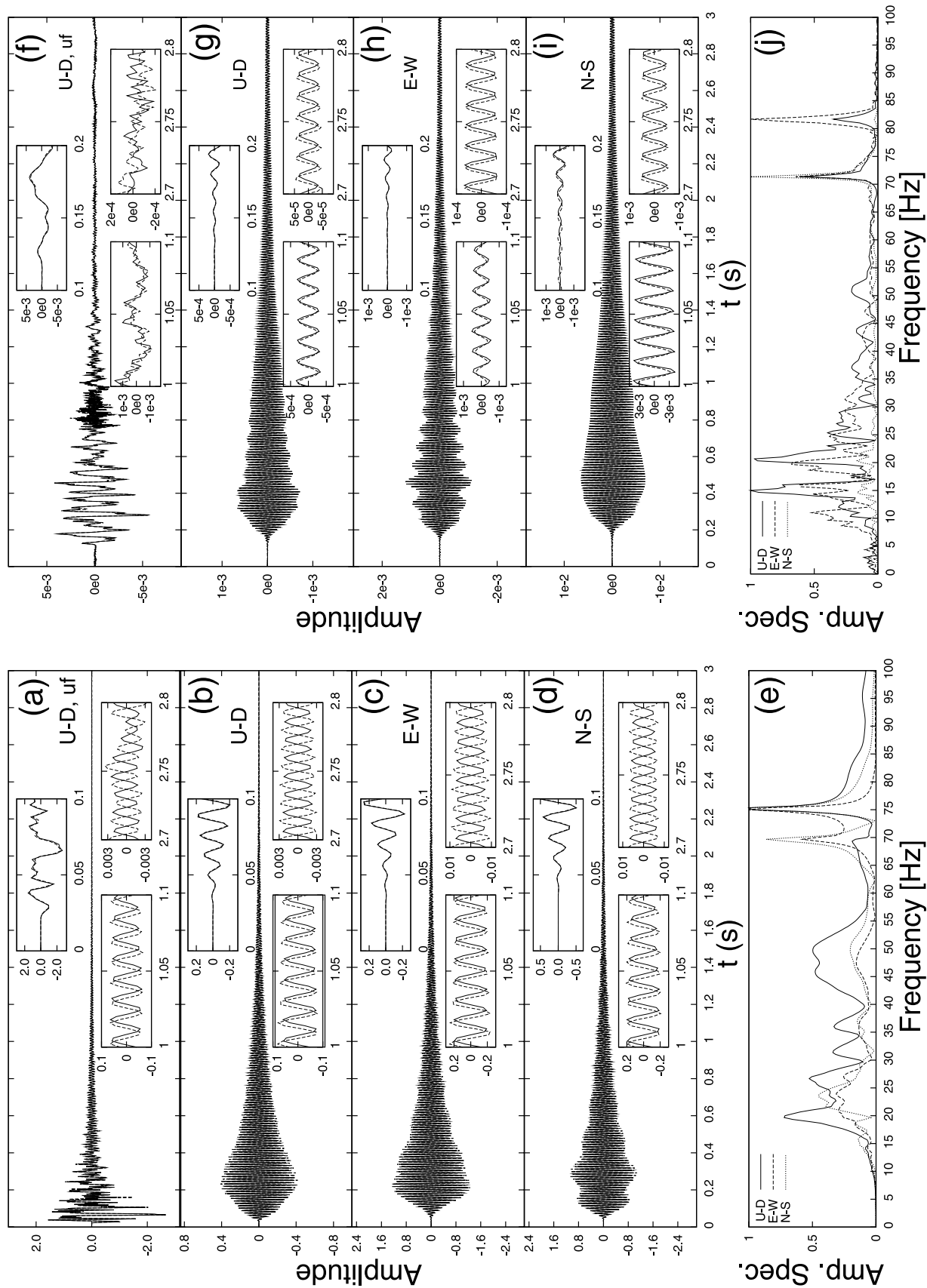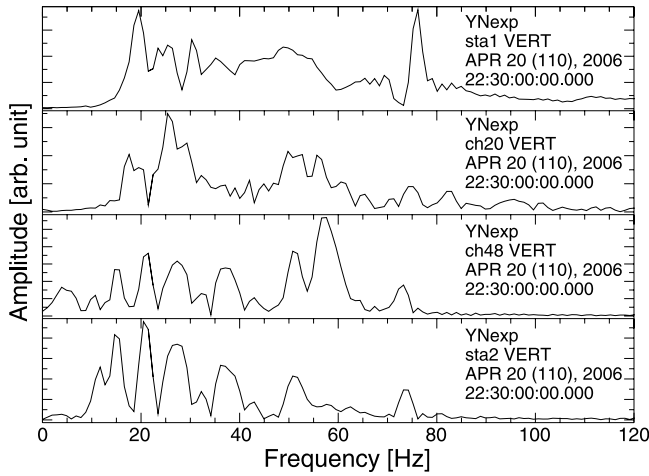
Figure 3

Figure 4. Amplitude spectra calculated from the first 0.512 second of the waveforms recorded at station 1, geophone channels 20, 48 and station 2. Note the similarity between the spectra of channel 48 and station 2.

and dashed line for the 22:30 of 8 April shot). The early parts of the aligned seismographs are almost identical, while an obvious phase shift was found in the later (coda) part (insets in Figure 3). To use the coda wave interferometry to measure subtle changes in the velocity field, we compute the cross correlation between the first seismogram and each subsequent seismogram within a 0.1 second moving time window and a running step of 0.1 second. The time delay $\tau(t)$ is obtained when the maximum cross correlation, $C_m(t)$, is reached.

[14] Many factors could affect the precision in the time delay (τ) estimation. There is a theoretical lower limit on the achievable precision for any unbiased time delay estimators. This limit is known as the Cramer-Rao Lower Bound (CRLB) [e.g., *Quazi*, 1981; *Carter*, 1987]. The CRLB prediction of the standard deviation in the time delay estimates, σ_τ^m, is [*Quazi*, 1981; *Walker and Trahey*, 1995; *Silver et al.*, 2007]:

$$\sigma_\tau \geq \sigma_\tau^m = \sqrt{\frac{3}{2\pi^2 T f_0^3 (B^3 + 12B)}\left(\frac{1}{\rho^2}\left(1 + \frac{1}{SNR^2}\right)^2 - 1\right)}. \quad (1)$$

[15] Here, f_0, B, ρ, SNR, T are the dominant frequency, fractional frequency bandwidth (bandwidth over the dominant frequency), source waveform similarity, signal-to-noise ratio and kernel window length, respectively. In our case, we have $f_0 \approx 77$ Hz, $B \approx 0.1$, $SNR \gg 1$, and $T = 0.1$ second. We measured the source waveform similarity ρ by averaging maximum cross-correlation coefficient $C_m(t)$ over all the

consecutive time windows. The average cross-correlation coefficient $\overline{C}$ is shown in Figure 5. The coda wave records exhibit high similarity, and most of the average correlation coefficient $\overline{C} > 0.9$. We also observe a drop in similarity immediately after the rainfall that started from hour 485 especially for station 2.

[16] Because of the high waveform similarity shown in Figure 5, we set ρ to 1. Thus equation (1) can be simplified as:

$$\sigma_\tau^m = \frac{1}{2\pi f_0 \text{SNR}} \sqrt{\frac{1}{f_0 TB}} \quad (2)$$

For a given SNR of 20, we obtained a σ_τ^m of $\sim 1 \times 10^{-4}$ second. Since travel times of coda waves are in the order of 1 second, the standard deviation of the normalized time delay, $\sigma_{\tau/t}^m = \sigma_\tau^m/t$, is estimated to be $\sim 1 \times 10^{-4}$.

[17] The sampling intervals of the data were 2 ms. To obtain sub-sample precision for the time delay estimation, three different methods were applied to the data: (1) a linear interpolation of the seismograms; (2) a cubic spline interpolation of the seismograms; and (3) a cosine curve fitting of the correlation function [e.g., *Céspedes et al.*, 1995]. In method (1) and (2) the seismograms were interpolated to a sampling interval of 0.1 ms (i.e., 20 times finer than the original sampling interval). No discernible difference was found among the three methods.

[18] Two examples of the time delay $\tau(t)$ measured at station 1 are shown in Figure 6. They are plotted as a function of the elapse time, t. The measured time delays are well-defined linear functions of the elapse time over the entire experiment period. It has been theoretically [e.g., *Snieder*, 2006] and numerically [e.g., *Niu et al.*, 2003] proved that when and only when there is a change in the bulk velocity field, τ and t will exhibit a linear relationship. The fractional change of velocity, $\delta v/v$, is equal to the negative slope $(-\tau/t)$ of the lines (Figure 6).

[19] We employed L_2 regression [e.g., *Press et al.*, 1995] to determine the velocity variation (i.e., the slope of τ/t). The regression allows for a direct estimation of the uncertainty in the measured velocity variation. When only the first arrival is used, it is very difficult to estimate the errors directly other than using the CRLB to obtain a theoretical lower bound [e.g., *Snieder et al.*, 2002; *Grêt et al.*, 2006b]. The regression gives an uncertainty of $\sim 10^{-4}$ in our $\delta v/v$ estimates.

4. Temporal Changes in Velocity and Possible Interpretation

[20] We used two methods to calculate the temporal velocity variation. The first one used the first shot fired at

Figure 3. Examples of seismograms recorded at stations (a-d) 1 and (f-i) 2 from two shots fired at 22:30 pm of 7 April 2006 (solid line) and 22:30 pm of 8 April 2006 (dashed line). Raw data recorded at the vertical components are shown in Figures 3a and 3f for stations 1 and 2, respectively. Figures 3b-3d and 3g-3i are the bandpass-filtered seismograms with pass bands of 73–78 Hz and 69–75 Hz for stations 1 and 2, respectively. Insets show the enlarged first arrivals and coda waves in two time windows. Notice that the waveforms of the first arrivals from the two shots are almost identical, while the coda waves show apparent phase shifts and some waveform dissimilarity between the two shots. The normalized amplitude spectra of the 22:30 pm of 7 April shot are shown in Figures 3e and 3j.
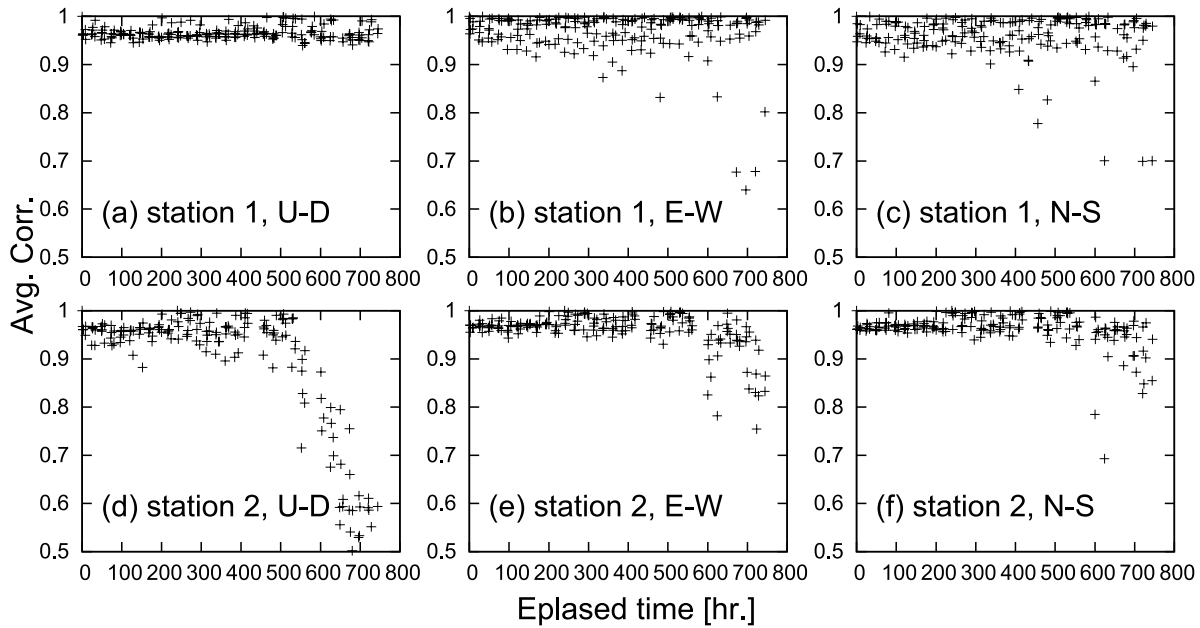
Figure 5. The temporal variation of the average cross-correlation coefficient, $\overline{C}_m$, between the first shot and the subsequent shots recorded at the three components of (a–c) station 1 and (d–f) station 2.

22:30 pm of 7 April as the reference and all the resulting temporal variation is the accumulative changes occurred after the first shot. The second method calculated the small variations between two consecutive shots and these variations were finally integrated to obtain the cumulative changes with respect to the first shot. No prominent difference was found between the results calculated from the two methods. Somehow the result from the second method appears to be more stable, probably due to the better similarity between the consecutive pairs.

[21] At station 2 we were unable to obtain stable estimations on velocity variation from any of the three components after the rainfall, due to poor waveform similarity (Figure 5). $\delta v/v$ estimated from the three components of station 1 and station 2 is shown in Figure 7. The average standard deviation of all the measurements is $\sim 3 \times 10^{-4}$, which coincides quite well with the theoretical prediction by equation (2). Estimations from the three components of station 1 coincide with each other remarkably well, and the results from station 2 also show a general agreement with them. The excellent internal consistency shown in Figure 7 is a good indication of the high reliability in our estimates.

[22] From the results of the regular experiment, we observed clear daily cycles in the velocity perturbation. The daily change of velocity is approximately one tenth of percent. Besides the daily cycles, we also saw a linear trend in the data which show a rapid increase about 16 hours after the rainfall. On the basis of the slope of the linear trend, we divided the 1-month period into 3 different stages: stages I, II and III corresponding to the periods before, during and after the abrupt change in velocity (Figure 7). Two daily cycles can be also found in the results of the densely sampled experiment, which are shown in bottom of Figure 7. The variation amplitude reaches as much as 1.5%. This is the largest perturbation that has been observed so far. It is about 5 to 10 times larger than the previous reports (see Table 1 in the study by *Yamamura et al.* [2003]).

4.1. Effect of Temperature

[23] It is well known that most of the electronic systems have very strong temperature dependency. The air temperature recorded at stations KM and YL are shown in Figure 7. The temperature records coincide with each other. Since our experimental site is located between the two stations KM and YL, it is reasonable to assume that the air temperature in the experimental site follows the same tendency as in KM and YL. Although the temperature records also show a daily variation, there is a two-hour phase shift between the temperature records and measured velocity perturbation.

[24] As we mentioned before, there are two major non-random errors in the time delay measurement: error in triggering time and drift of the digitizer's base clock.
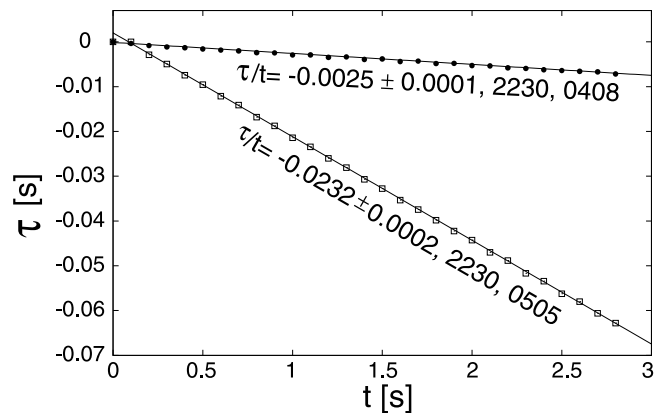

Figure 6. Time delay, τ, is plotted as a function of elapse time after the first arrival. Vertical component of the station 1 from two subsequent shots fired at 22:30 pm of 8 April and 22:30 pm of 5 May is used in estimating the time delays.
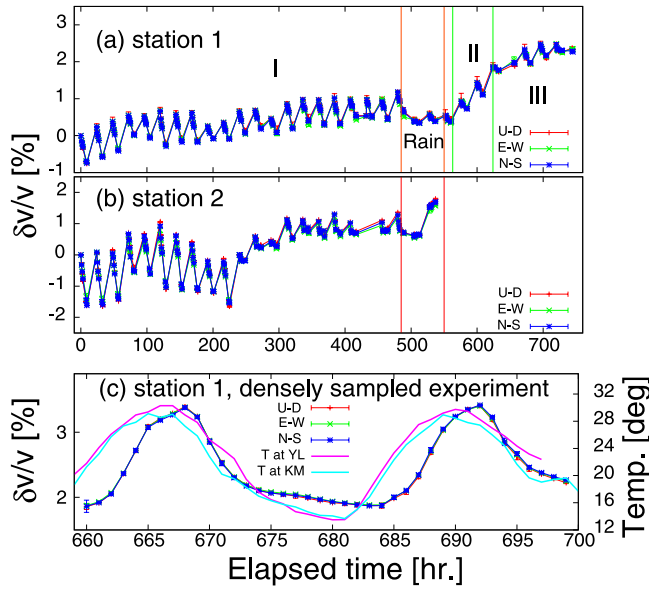
Figure 7. Estimated time delay at (a) station 1 and (b) station 2 over the 1-month period. Estimates using recordings at station 1 from the densely sampled experiment are shown in Figure 7c, together with the temperature records of KM and YL. Uncertainties in the $\delta v/v$ measurements are 3.6×10^{-4}, 2.0×10^{-4}, 1.5×10^{-4}, 3.5×10^{-4}, 6.0×10^{-4} and 4×10^{-4} for the U-D, E-W and N-S components of stations 1 and 2, respectively. The three different stages used in the linear regression are marked by I, II, and III, respectively.

Temperature is expected to affect both the performance of triggering and the digitizer's base clock. Since we aligned the seismograms along the first arrival and measured the differential travel time of the coda waves with respect to the first arrival, our measurement should be insensitive to triggering time errors. Our measurements on the time delay are, however, sensitive to the accuracy of the sampling intervals which might be affected by temperature fluctuation. When a signal f was sampled with interval Δ' perturbed from the preset interval Δ (2 ms in our case) as $f(n\Delta')$, $n = -\infty \cdots \infty$. The Fourier transform calculated with the preset sampling interval is:

$$
\begin{aligned}
H'(\omega) &= \sum_{n=-\infty}^{\infty} f(n\Delta') \exp[-i\omega n\Delta] \\
&= \sum_{n=-\infty}^{\infty} f(n\Delta') \exp[-i(\omega\Delta/\Delta')n\Delta'] = H(\omega\Delta/\Delta') \quad (3)
\end{aligned}
$$

Here, ω is angular frequency, and H is the Fourier spectrum of f when sampled with preset sampling interval. From equation (3), we can see that the perturbation in sampling interval will result in a rescaling of the Fourier spectrum by a factor of Δ/Δ'. As discussed in the last section, a change in the bulk velocity of the medium will also lead to a linear change in time delay, similar to those expected from a shift in the sampling interval.

[25] The amplitude spectra of the E-W component recorded at station 1 are shown in Figure 8a. We only

showed those calculated from the densely sampled experiment. There are three notable peaks at ~20, 72 and 77 Hz, in the amplitude spectra. The positions of those three peaks were marked with solid lines in Figure 8. The 20 Hz first arrival peak remains unchanged over the entire 40 hours period, while significant changes can be found in the two high-frequency peaks (Figure 8b). This was also confirmed from the other two components of station 1. If the sampling rate was perturbed by temperature fluctuation, the locations of all the three peaks should be modified in a similar way, which is not observed here. Furthermore, the digitizer that we used in the experiment has a working temperature from $-20°C$ to $50°C$. The variation in central frequency is expected to be less than several ppm (Beijing Gangzhen Mechanical and Electronic Technology Co., Ltd., personal communication, 2006). Thus we conclude that the changes in the position of the high-frequency peaks are unlikely to be caused by temperature fluctuation.

[26] Frequency variation of the 77 Hz peak follows the same tendency as the measured velocity change (Figure 8b). The total frequency change over the 40 hours period is 1.2 Hz. The fractional frequency change is thus ~1.5%, which coincides well with the amplitude of the observed velocity variation in the same period.
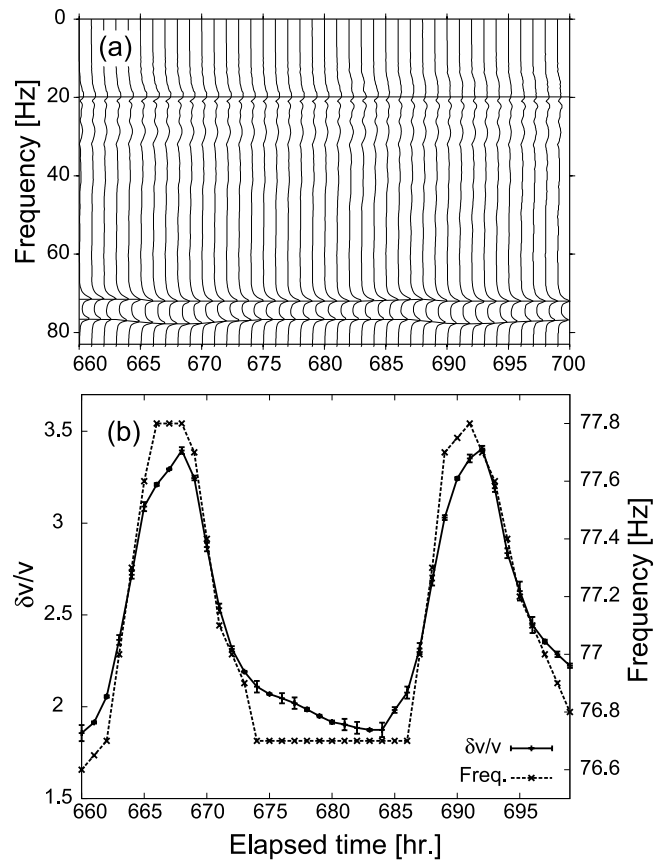

Figure 8. (a) Normalized amplitude spectra of E-W component of station 1. (b) A comparison of the frequency fluctuation of the coda wave peak and the estimated velocity perturbation. Notice the remarkably good agreement between the two different parameters.
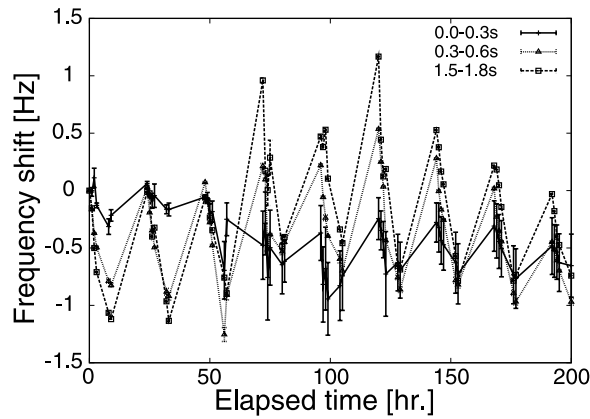
Figure 9. Temporal variations in frequency of the ~72 peak observed at the vertical component of station 2 measured from three different coda window: 0.0–0.3, 0.3–0.6, 1.5–1.8 seconds. Variations are calculated with respect to the first shot, see text for details.

[27] In fact, the observed variations in frequency can be used to argue that the coda waves are not instrument related auto-oscillations. If the coda waves were instrument related auto-oscillations and the observed variations were induced by temperature, then we would expect to obtain the same amount of frequency shift regardless which time window of the coda are used in the measurement. This is, however, not true. Frequency variations of the ~72 Hz peak recorded at station 2 measured from three time windows (0.0−0.3; 0.3−0.6; 1.5−1.8 seconds) are shown in Figure 9. There are significant differences among the measurements derived from the three time windows, indicating that the observed temporal variations are not originated from temperature changes which should be negligible within 2 seconds.

4.2. Interpretation of the Observed Velocity Variation

[28] Ground water levels have long been observed to be sensitive to the subsurface stress state [e.g., *Montgomery and Manga*, 2003]. The water level recorded at XS station 1.2 km south to the experiment site is shown in Figure 10a, together with the velocity perturbation measured from the U-D component of station 1. For comparison we also showed other geodetic data: barometric pressure and relative gravity recorded at station KM in Figure 10. The synthetic areal strain $e_{NS} + e_{EW}$ calculated with ETERNA 3.30 [*Wenzel*, 1996] are also included (Figure 10d). The synthetic areal strain correlates almost perfectly with the observed gravity (Figures 10c and 10d). The areal strain used here is defined as compressional. A positive compressional strain means areal consumption. The variation of the
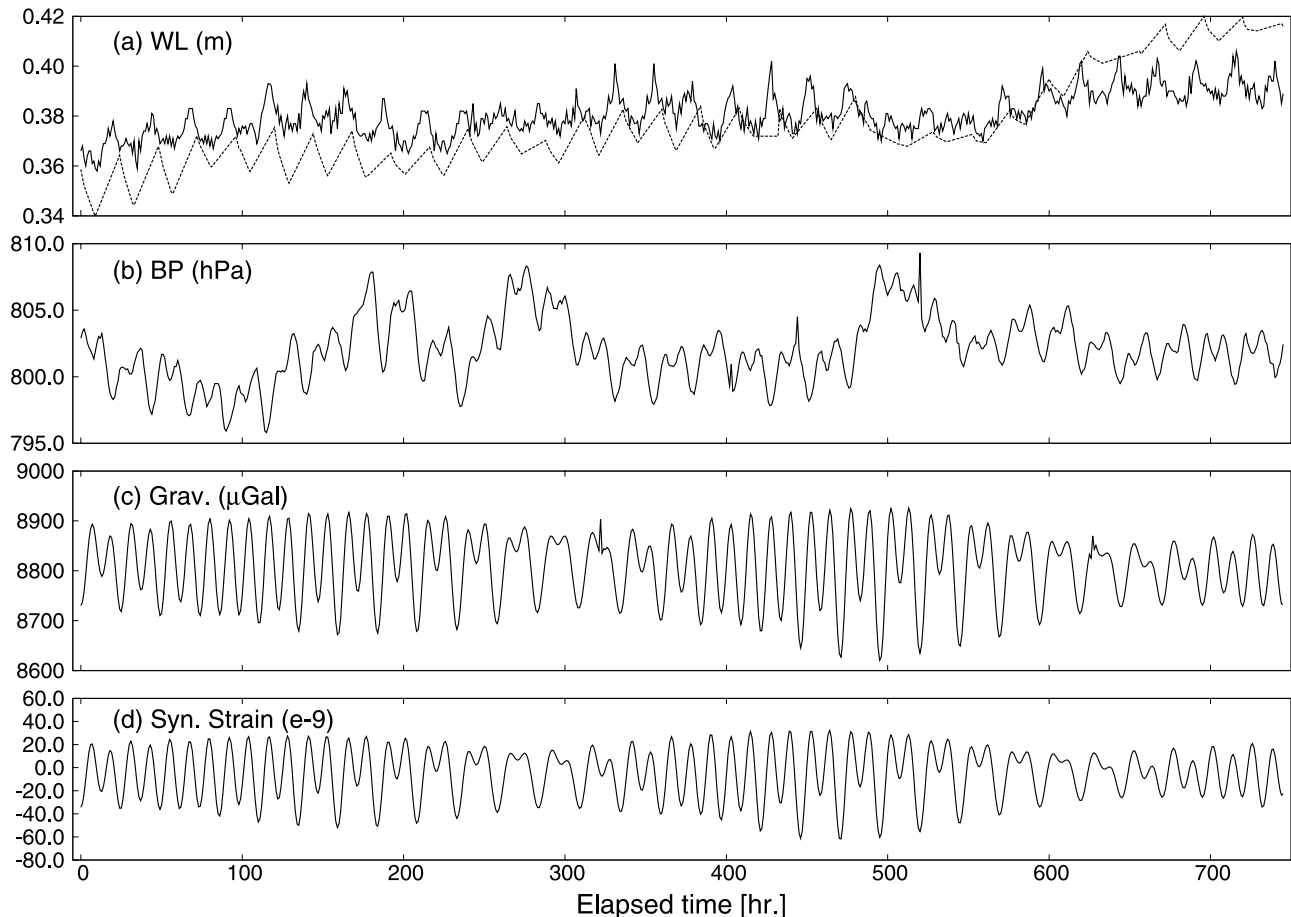

Figure 10. A comparison of the estimated $\delta v/v$ with (a) ground water level, (b) barometric pressure, (c) relative gravity, and (d) the calculated area strain. In Figure 10a, $\delta v/v$ is shown in dashed line. Notice the good correlation between $\delta v/v$ and water level.
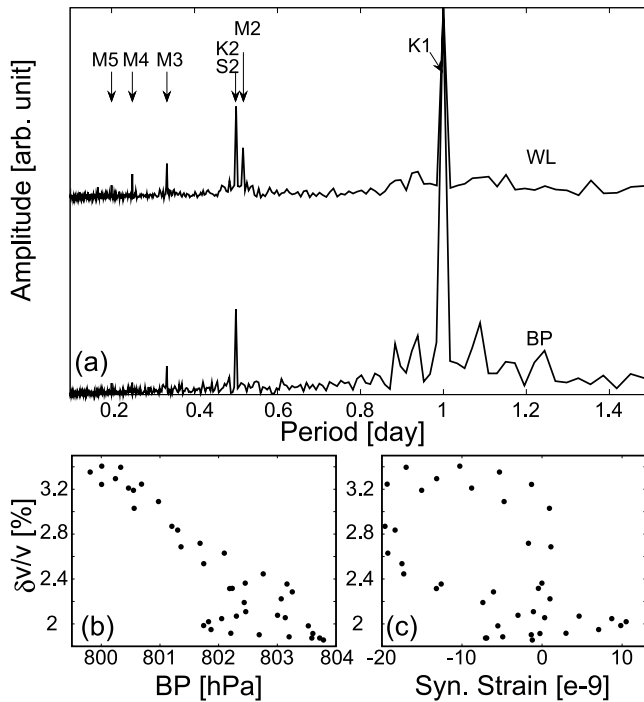
Figure 11. (a) Amplitude spectra (in arbitrary unit) of the water level (wl) recorded at XS and barometric pressure recorded at KM. Various modes corresponding to the solid Earth tide (e.g., diurnal and semi-diurnal) can be identified. Velocity changes shown as a function of (b) barometric pressure and (c) synthetic tidal strain.

barometric pressure is in the order of 10^3 Pa. The bulk modulus used in previous studies [e.g., *Reasenberg and Aki*, 1974; *Yukutake et al.*, 1988; *Yamamura et al.*, 2003] ranges from 2 to 50 GPa. With an assumed bulk modulus of 5 GPa, the solid earth tide applied areal stress variation, as the product of areal strain variation and bulk modulus, is found to be ~5 × 10^2 Pa, which is about two times smaller than the changes in barometric pressure.

[29] Tidal modes with periods of one day (K1), half day (M2 and S2/K2), 1/3 day (M3), 1/4 day (M4) and 1/5 day (M5) can be observed in the Fourier spectra of the water level records (Figure 11a). Diurnal and semi-diurnal modes are also shown in the spectra of barometric pressure (Figure 11a). Although it is not shown here, the gravity data also contain these modes. Since our regular experiment was conducted with uneven sampling intervals, we cannot apply the Fourier analysis to the estimated velocity variation to confirm these different tidal modes. Daily cycles with a velocity perturbation of 10^{-3} to 10^{-2}, however, are clearly shown in the results from both the regular and densely sampled experiments.

[30] Throughout the experiments, there is a good correlation between the estimated velocity perturbation and the observed ground water level (Figure 10a). In general, water level is mainly affected by the applied stress field including the barometric pressure and solid earth tide [e.g., *Spane*, 2002]. The linear relationship between the velocity and ground water level thus implies these two loadings might be responsible for the velocity perturbation. On the other

hand, the estimated velocity changes showed a clear negative-correlation with barometric pressure (Figure 11b), but no obvious dependence on the synthetic tidal strain (Figure 11c). This is consistent with the observations of *Silver et al.* [2007].

[31] A L2-norm linear regression was employed to estimate the velocity dependency on the barometric pressure (*BP*):

$$\delta v/v = \alpha_1 \cdot t + \alpha_2 \cdot BP \qquad (4)$$

On the basis of the long-term linear trend in the velocity perturbation measured from station 1, we have divided the experiment period into three stages. The regression was thus conducted separately for these different stages. Figure 12 shows the fitting results, and it is clear that the observed velocity perturbation can be fitted reasonably well. The coefficients, α_1 and α_2 at the three stages are summarized in Table 1. We have only 14 data points used in the regression for fitting the results of stage II. Thus the resulting fitting is thought to be less reliable. The two coefficients α_1 and α_2, correspond to long-term linear trend and velocity sensitivity to the barometric pressure, respectively. The linear trend at stages I and III are of 10^{-5} hr^{-1}. If this is induced by long-term stress changes, the corresponding strain rate is $\alpha_1/(\alpha_2 K)$, where K is the bulk modulus. We estimate it in the order of 10^{-6} yr^{-1}. Recent GPS study [*Zhang et al.*, 2004] found that the study region is under expansion with an annual rate of ~10^{-8} yr^{-1}. Thus tectonic stress is unlikely to be the cause of the observed linear trend.

5. Discussion

[32] Velocity dependence on barometric pressure for stage I is estimated in the order of 10^{-6} Pa^{-1}. The value agrees reasonably well with most of the previous subsurface measurements [e.g., *Yamamura et al.*, 2003; *Silver et al.*, 2007]. Velocity dependence on barometric pressure appears to be affected prominently by precipitation associating with the rainfall. It increased by a factor of 10 from ~-3.7×10^{-6} Pa^{-1} in stage I to -3.8×10^{-5} Pa^{-1} in stage III. An increase in stress sensitivity after the rain was also observed by *Silver et al.* [2007], which was interpreted as a result of weakening of the media. The stress sensitivity of velocity is always attributed to opening/closure of microcracks embedded in the media. How microcracks respond to the confining stress is likely controlled by many factors including physical properties (stiffness, crack density, permeability) of crustal rocks, and amount of fluids permeated in the media.

[33] Our measured velocity perturbation is an average of velocity changes occurring at different depths. As they are generated by multiple scattering/reflection, coda waves usually have very complicated ray paths, which are almost impossible to trace. It is thus difficult to estimate penetrating depths based on ray paths. The sampling depth, on the other hand, must be greater than the sizes of the scatterers, which should be comparable with the wavelength of the coda waves [e.g., *Aki and Richards*, 1980; *Niu et al.*, 2003]. On the basis of a dominant frequency of 77 Hz and a P-wave velocity of 2.8 km/s, we estimated the penetrating depth to be a few tens of meters. As confining stress increases with depth, crack density decreases with depth and therefore
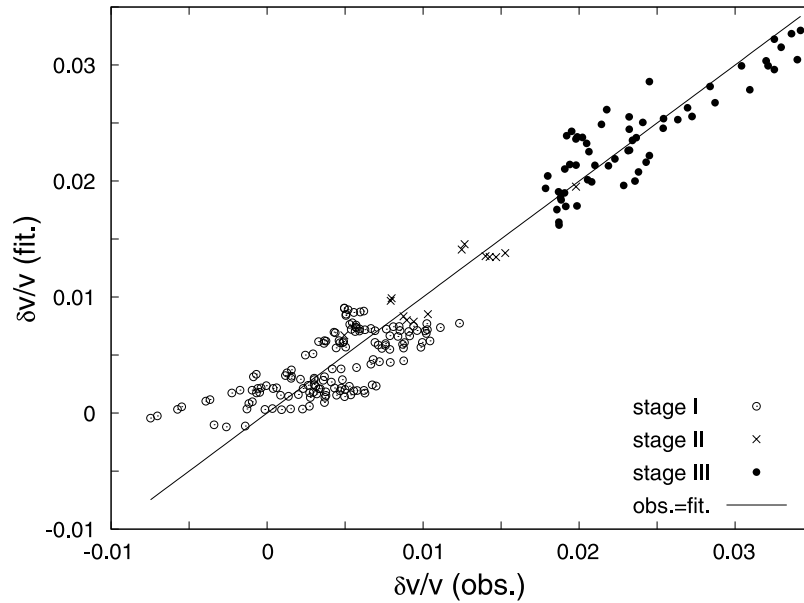
Figure 12. The best fitting predictions of $\delta v/v$ are plotted against the observed $\delta v/v$. Data from stages I, II and III are indicated by open circles, crosses, and solid circles, respectively.

stress sensitivity should also decrease with depth. The observed large stress sensitivity must be related to the shallow depth that the coda waves have sampled. It may also explain why the velocity perturbation is so sensitive to the rainfall precipitation.

[34] While all the previous studies measured stress-induced perturbations in the P wave velocity, our estimates based on coda waves probably reflect changes mostly in the S-wave velocity, as the coda consists mainly of multiple scattered S wave energy. On the basis of the study by *Snieder et al.* [2002], the measured velocity perturbation here is a weighted summation of perturbations of $\delta v_p/v_p$ and $\delta v_s/v_s$ as $\delta v/v = 0.91\delta v_s/v_s + 0.09\delta v_p/v_p$. Both theoretically calculation [*O'Connell and Budiansky*, 1974] and laboratory study [e.g., *Dvorkin et al.*, 1996] have found that S wave velocity also exhibit a stress dependence.

[35] A cracked medium is generally envisioned as a two phase medium composed of solid framework and cracks saturated with fluids (gas or liquid). The experiment site is located on the top of an anti-cline, where tensile stress prevails and cracks may interconnect with each other through some narrow throats (Figure 13). Velocity was observed to be related to the effective stress (defined as confining stress minus pore pressure $p_e = p_c - p_p$) [e.g., *Toksöz et al.*, 1976]. It is obvious that tidal loading affect the confining stress only. The effect of barometric pressure is more complicated. It affects both the confining stress and pore pressure and consequently the effective stress in two contrary ways. It raises the confining pressure through increasing loads on the solid framework. Meanwhile,

depending on the connectivity of the cracks, it can also increase the pore pressure through compressing the fluids embedded in the crack network. *Silver et al.* [2007] observed negative and positive mixed sensitivities on barometric pressure, which they explained as the near-field and far-field effects, respectively. For a short baseline a raise of the pore pressure appears to be the dominant factor which increases average crack density, and therefore decreases the seismic velocities of the medium. This could be also true for our case, as we observed a negative stress sensitivity
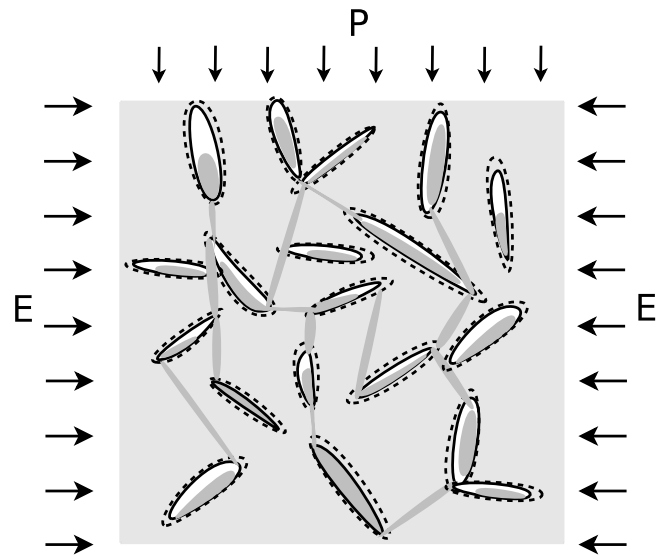

Figure 13. A cartoon shows the preferred crack model. Cracks are connected with each other, and the network opens to the barometric pressure. An increase of barometric pressures leads to an increase in crack density, which opens more space to the fluids and results in a decrease of fluid saturation that affects the seismic velocities.

Table 1. Fitting Results for Different Stages

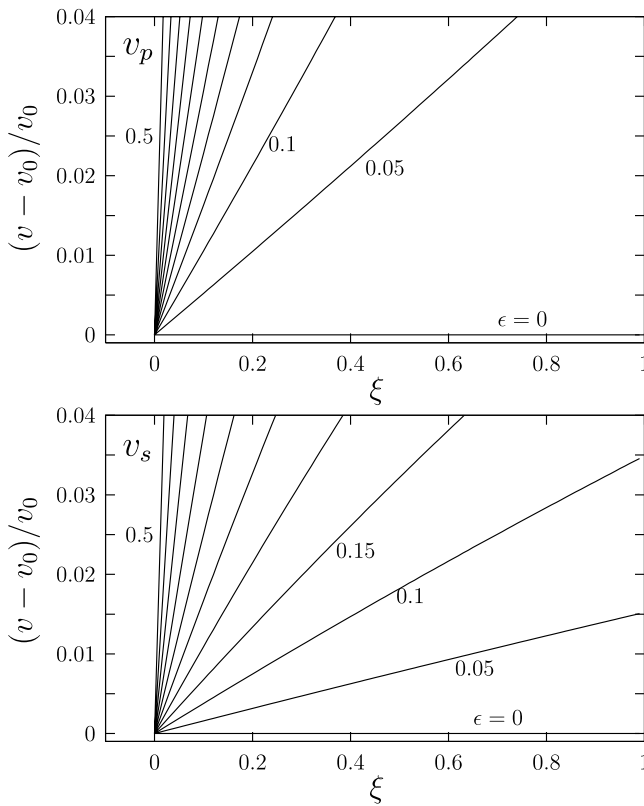| Parameter	Stage I	Stage II	Stage III
α_1 (hour^{-1})	1.8×10^{-5}	1.9×10^{-4}	4.9×10^{-5}
α_2 (Pa^{-1})	-3.7×10^{-6}	-1.0×10^{-5}	-3.8×10^{-5}

Figure 14. P and S wave velocities are shown as a function of crack density ε and fractional saturation ξ. The calculation is based on equations (17), (18) and (28) of the study by *O'Connell and Budiansky* [1974]. Values shown are the normalized deviations from those with dry cracks.

to the barometric pressure throughout the entire experiment period. Other mechanism might be also involved to produce the large increase in the sensitivity associating with the rainfall.

[36] Besides being sensitive to the applied stress, P and S velocities of rocks are also known to change with the fraction of fluids in the embedded cracks [e.g., *Murphy*, 1984]. *Yukutake et al.* [1988] argued that the in-situ subsurface velocities are also affected by the partial saturation. *O'Connell and Budiansky* [1974] developed a theory to calculate seismic velocity of a medium with penny shaped cracks. Velocity appears to be a non-linear function of crack density, ε, and fraction of saturation, ξ. On the basis of their theory, we calculated the P and S wave velocity for an assumed medium with a crack density ($0 \leq \varepsilon \leq 0.5$) and saturation ($0 \leq \xi \leq 1$). The results are shown in Figure 14. With a crack density of $\varepsilon = 0.5$, we need only 1% change in saturation to produce a 2% increase in v_p and v_s. For $\varepsilon = 0.1$, the required change in saturation rate is about 40−50% for producing the same amount of velocity increase. Since the increase of the stress sensitivity is observed right after the rainfall, it is plausible to argue that part of the observed velocity change is related in the change of fluid saturation resulting from precipitation infiltrating into the rocks. The existence of fluids thus tends to be able to enhance the stress sensitivity, making it possible to measure stress variations at

seismogenic depth as fluids have been identified at depths as much as 4 km or even more [*Yamamura et al.*, 2003].

6. Conclusions

[37] We conducted a 1-month field experiment in the Yunnan Province of southeast China to measure changes in the subsurface velocity. Velocity was measured 6 times per day along two baselines with a source-receiver distance of ∼10 m and 250 m. Using the coda wave interferometry technique, we were able to obtain a precision of 10^{-4} in measuring the fractional velocity change with commercial short-period seismometers. We observed a daily variation of ∼10^{-3} to 10^{-2} in the velocity perturbation. An increase of seismic velocity was also observed right after a continuous 3-day rainfall.

[38] The observed velocity perturbation tracks very well with the ground water level recorded near the experiment site. Changes in barometric pressure were attributed for the velocity perturbation. We found a negative stress sensitivity of 10^{-6} for barometric pressure. The negative sensitivity can be explained by its effect on the effective stress that controls the crack density in crustal rocks. There is a drastic increase of the stress sensitivity to barometric pressure after the rainfall. We interpreted this increase as the combination effect of changes in effective stress and fluid saturation in cracks.

References

Aki, K. (1969), Analysis of the seismic coda of local earthquakes as scattered waves, *J. Geophys. Res.*, *74*(2), 615–631.
Aki, K., and B. Chouet (1975), Origin of coda waves: Source, attenuation, and scattering effects, *J. Geophys. Res.*, *80*(23), 3322–3342.
Aki, K., and P. G. Richards (1980), *Quantitative Seismology: Theory and Methods*, W. H. Freeman, New York.
Birch, F. (1960), The velocity of compressional waves in rocks to 10 kilobars, Part 1, *J. Geophys. Res.*, *65*, 1083–1102.
Birch, F. (1961), The velocity of compressional waves in rocks to 10 kilobars, Part 2, *J. Geophys. Res.*, *66*, 2199–2224.
Carter, G. C. (1987), Coherence and time delay estimation, *Proc. IEEE*, *75*(2), 236–255.
Céspedes, I., Y. Huang, J. Ophir, and S. Spratt (1995), Methods for estimation of subsample time delays of digitized echo signals, *Ultrason. Imaging*, *17*, 142–171.
De Fazio, T. L., K. Aki, and J. Alba (1973), Solid earth tide and observed change in the in situ seismic velocity, *J. Geophys. Res.*, *78*, 1319–1322.
Dvorkin, J., A. Nur, and C. Chaika (1996), Stress sensitivity of sandstones, *Geophysics*, *61*(2), 444–455.
Grêt, A. A., R. Snieder, R. C. Aster, and P. R. Kyle (2005), Monitoring rapid temporal change in a volcano with coda wave interferometry, *Geophys. Res. Lett.*, *32*, L06304, doi:10.1029/2004GL021143.
Grêt, A. A., R. Snieder, and U. Özbay (2006a), Monitoring in situ stress changes in a mining environment with coda wave interferometry, *Geophys. J. Int.*, *167*(2), 504–508.
Grêt, A. A., R. Snieder, and J. Scales (2006b), Time-lapse monitoring of rock properties with coda wave interferometry, *J. Geophys. Res.*, *111*, B03305, doi:10.1029/2004JB003354.
Herraiz, M., and A. F. Espinosa (1987), Coda waves: A review, *Pure Appl. Geophys.*, *125*, 499–577.

Leary, P. C., P. E. Malin, R. A. Phinney, T. Brocher, and R. VonCollin (1979), Systematic monitoring of millisecond travel time variations near Palmdale, California, *J. Geophys. Res.*, *84*, 659–666.

Matsumoto, S., K. Obara, K. Yoshimoto, T. Saito, A. Ito, and A. Hasegawa (2001), Temporal change in P-wave scatterer distribution associated with the M6.1 earthquake near Iwate volcano, northeastern Japan, *Geophys. J. Int.*, *145*, 48–58.

Montgomery, D. R., and M. Manga (2003), Streamflow and water well responses to earthquakes, *Science*, *300*, 2047–2049.

Murphy, W. F. (1984), Acoustic measures of partial gas saturation in tight sandstones, *J. Geophys. Res.*, *89*, 11,549–11,559.

Niu, F., P. G. Silver, R. M. Nadeau, and T. V. McEvilly (2003), Migration of seismic scatterers associated with the 1993 Parkfield aseismic transient event, *Nature*, *426*, 544–548.

Nur, A. (1971), Effects of stress on velocity anisotropy in rocks with cracks, *J. Geophys. Res.*, *76*, 2022–2034.

O'Connell, R. J., and B. Budiansky (1974), Seismic velocities in dry and saturated cracked solids, *J. Geophys. Res.*, *79*, 5412–5426.

Poupinet, G., W. L. Ellsworth, and J. Frechet (1984), Monitoring velocity variations in the crust using earthquake doublets: An application to the Calaveras faults, California, *J. Geophys. Res.*, *89*, 5719–5731.

Press, W. H., S. A. Teukolsky, W. T. Vetterling, and B. P. Flannery (1995), *Numerical Recipes in C: The Art of Scientific Computing*, 2nd ed., Cambridge Univ. Press, Cambridge.

Quazi, A. (1981), An overview on the time delay estimate in active and passive systems for target localization, *IEEE Trans. Acoust., Speech Signal Process.*, *29*(3), 527–533.

Ratdomopurbo, A., and G. Poupinet (1995), Monitoring a temporal change of seismic velocity in a volcano: Application to the 1992 eruption of Mt. Merapi (Indonesia), *Geophys. Res. Lett.*, *22*, 775–778.

Reasenberg, P., and K. Aki (1974), A precise, continuous measurement of seismic velocity for monitoring in situ stress, *J. Geophys. Res.*, *79*, 399–406.

Sens-Schönfelder, C., and U. Wegler (2006), Passive image interferometry and seasonal variations of seismic velocities at Merapi Volcano, Indonesia, *Geophys. Res. Lett.*, *33*, L21302, doi:10.1029/2006GL027797.

Silver, P. G., T. M. Daley, F. Niu, and E. L. Majer (2007), Active source monitoring of crosswell seismic travel time for stress induced changes, *Bull. Seismol. Soc. Am.*, *97*, 281–293.

Simmons, G. (1964), Velocity of shear waves in rocks to 10 kilobars 1, *J. Geophys. Res.*, *69*, 1123–1130.

Snieder, R. (2006), The theory of coda wave interferometry, *Pure Appl. Geophys.*, *163*, 455–473, doi:10.1007/s00024-005-0026-6.

Snieder, R., A. A. Grêt, H. Douma, and J. Scales (2002), Coda wave interferometry for estimating nonlinear behavior in seismic velocity, *Science*, *295*, 2253–2255.

Song, F., Y. Wang, W. Yu, Z. Cao, X. Shen, and J. Shen (1998), *Xiaojiang Active Fault Zone (in Chinese)*, Seismological Press, Beijing, China.

Spane, F. A. (2002), Considering barometric pressure in groundwater flow investigations, *Water Resour. Res.*, *38*(6), 1078, doi:10.1029/2001WR000701.

Toksöz, M. N., C. H. Cheng, and A. Timur (1976), Velocities of seismic waves in porous rocks, *Geophysics*, *41*, 621–645.

Walker, W. F., and G. Trahey (1995), Limits on the performance of near field phase aberration correction, *IEEE Ultrason. Symp.*, *2*, 1461–1465.

Walsh, J. B. (1965), The effect of cracks on the compressibility of rocks, *J. Geophys. Res.*, *70*, 381–389.

Wegler, U. (2004), Diffusion of seismic waves in a thick layer: Theory and application to Vesuvius volcano, *J. Geophys. Res.*, *109*, B07303, doi:10.1029/2004JB003048.

Wegler, U., B.-G. Lühr, R. Snieder, and A. Ratdomopurbo (2006), Increase of shear wave velocity before the 1998 eruption of Merapi volcano (Indonesia), *Geophys. Res. Lett.*, *33*, L09303, doi:10.1029/2006GL025928.

Wenzel, H.-G. (1996), The nanogal software: Earth tide data processing package ETERNA 3.30, *Bull. Inf. Mareés Terr.*, *124*, 9425–9439.

Yamamura, K., O. Sano, H. Utada, Y. Takei, S. Nakao, and Y. Fukao (2003), Long-term observation of in situ seismic velocity and attenuation, *J. Geophys. Res.*, *108*(B6), 2317, doi:10.1029/2002JB002005.

Yukutake, H., T. Nakajima, and K. Doi (1988), In situ measurements of elastic wave velocity in a mine, and the effects of water and stress on their variation, *Tectonophysics*, *149*, 165–175.

Zhang, P.-Z., et al. (2004), Continuous deformation of the Tibetan Plateau from global positioning system data, *Geology*, *32*, 809–812, doi:10.1130/G20554.1.

————————————
Y. Chen, B. Wang, and P. Zhu, Institute of Geophysics, China Earthquake Administration, No. 5 Minzudaxue South Road, Haidian District, Beijing 100081, China. (wangbs@cea-igp.ac.cn)

F. Niu, Department of Earth Science, Rice University, MS-126, 6100 Main Street, Houston, TX 77005, USA.

B. Wang, Earthquake Administration of Yunnan Province, 224 Beichen Av., Kunming 650224, China.